Development of a crystal collimation system for high-resolution ultra-small-angle X-ray scattering applications

Michael Sztucki,* Joachim Leonardon, Pierre Van Vaerenbergh, Jacques Gorini, Peter Boesecke and Theyencheri Narayanan
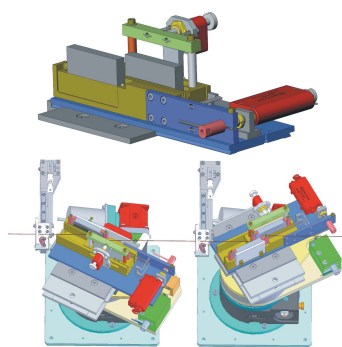
European Synchrotron Radiation Facility, CS 40220, 38043 Grenoble Cedex 9, France.
*Correspondence e-mail: sztucki@esrf.eu

Crystal collimation offers a viable alternative to the commonly used pinhole collimation in small-angle X-ray scattering (SAXS) for specific applications requiring highest angular resolution. This scheme is not affected by the parasitic scattering and diffraction-limited beam broadening. The Darwin width of the rocking curve of the crystals mainly defines the ultimate beam divergence. For this purpose, a dispersive Si-111 crystal collimation set-up based on two well conditioned pseudo channel-cut crystals (pairs of well polished, independent parallel crystals) using a higher-order reflection (Si-333) has been developed. The gain in resolution is obtained at the expense of flux. The system has been installed at the TRUSAXS beamline ID02 (ESRF) for reducing the horizontal beam divergence in high-resolution mesurements. The precise mechanics of the system allows reproducible alignment of the Bragg condition. The high resolution achieved at a sample–detector distance of 31 m is demonstrated by ultra-small-angle X-ray scattering measurements on a model system consisting of micrometre-sized polystyrene latex particles with low polydispersity.

1. Introduction

Ultra-small-angle X-ray scattering (USAXS) is a powerful technique for the structural elucidation of bulk materials over a size range from about a hundred nanometres to several micrometres (Bonse & Hart, 1965; Ilavsky *et al.*, 2009; Narayanan, 2014). In particular, a USAXS instrument employing an area detector has multiple advantages when investigating oriented samples and time-dependent processes (Kishimoto *et al.*, 2014; Narayanan *et al.*, 2018). Such a set-up imposes more stringent constraints on the beam collimation compared with traditional pinhole collimation widely used on small-angle scattering instruments (Narayanan, 2014). The main requirements on the collimation optics for synchrotron USAXS using area detectors are to provide high angular resolution and provide access to the smallest possible scattering angles. To achieve high resolution in momentum transfer of magnitude $q = (4\pi/\lambda)\sin(\vartheta/2)$ (where λ and ϑ are the X-ray wavelength and the scattering angle, respectively), the beam divergence and spot size at the detector should be as small as possible. To reach the lowest possible q values (USAXS), the parasitic halo around the direct beam has to be reduced to the minimum possible.

A highly collimated beam is usually obtained using multiple pairs of slits. However, the slit collimation is ultimately limited by scattering and beam broadening due to diffraction by the slits. This limitation may be overcome by crystal collimation that offers a viable alternative for reducing the beam diver-

gence (Ilavsky *et al.*, 2002, 2007). In this case, it is the width of the rocking curve of the crystals which limits the divergence (Bonse & Hart, 1965; Agamalian *et al.*, 2010). In addition, well conditioned crystals also aid in curtailing the parasitic background (Agamalian *et al.*, 1998; Sztucki *et al.*, 2007). The high brilliance of synchrotron sources and the high scattering power of typical well ordered systems (*e.g.* colloidal crystals), for which the high resolution is needed (Petukhov *et al.*, 2015), make the set-up useful despite the significant loss of flux due to multiple Bragg reflections.

In this paper, we report a dispersive Si-111 crystal collimation scheme based on two well conditioned pseudo channel-cut crystals using higher-order reflections. The performance of the set-up is demonstrated by experiments at the Time-Resolved Ultra-Small-Angle X-ray Scattering (TRUSAXS) beamline ID02 at the ESRF (Van Vaerenbergh *et al.*, 2016; Narayanan *et al.*, 2018). The vertical source size and divergence (FWHM) are very small ($\leq 20\ \mu$m and 7.6 µrad, respectively), whereas the horizontal beam size is about 950 µm with a divergence of 25 µrad (high-β section). Therefore, the horizontal beam size and divergence need to be curtailed for applications requiring high angular resolution and/or access to very small scattering angles.

The following sections describe the design and development of the crystal collimator set-up. The current installation at the TRUSAXS beamline is used to demonstrate the performance for horizontal beam conditioning and the mechanical stability of the set-up. It should also be mentioned that other Si diffraction orders could be envisaged. For example, use of Si-220 crystals together with the Si-111 monochromator simultaneously provide collimation and coherence-preserving harmonic rejection (Zhang *et al.*, 2018).

2. Crystal collimation

2.1. Principle

A highly collimated X-ray beam is required to access very small scattering angles and to achieve high angular resolution for small-angle-scattering experiments. The commonly used slit collimation is ultimately limited by diffraction. This is due to the fact that diffraction by an aperture increases the beam divergence, $\Delta\vartheta$, by about

$$\Delta\vartheta \simeq \lambda/d, \tag{1}$$

with d being the slit opening size. The increase of divergence is of the order of 1 µrad at $\lambda = 0.1$ nm and $d = 0.1$ mm. Therefore, the technical limit of collimation is reached when the broadening due to diffraction becomes equal to the size of the last collimation slit. This is the case for an aperture of

$$d_{\text{lim}} = (\lambda L)^{1/2}, \tag{2}$$

with L being the collimation length. At $\lambda = 0.1$ nm and $L = 23$ m, it results in $d_{\text{lim}} \simeq 50\ \mu$m.

On the other hand, crystal collimation is only limited by the Darwin width of the rocking curve of the crystals, of the order of 5 µrad using a Si-333 reflection at $\lambda = 0.1$ nm. The DuMond

diagram (DuMond, 1937) offers a convenient graphical means of visualizing the evolution of the two-dimensional distribution in angle (abscissa) and wavelength (ordinate) of X-rays undergoing multiple Bragg reflections as shown in Fig. 1(*a*). The diagonal strip of positive slope defines all rays of energy and angle which are accepted by a first set of crystals. The central dashed line follows the well known Bragg equation

$$\lambda = 2d\sin(\theta), \tag{3}$$

where θ is the Bragg angle and the width of the strip parallel to the abscissa represents the angular Darwin width.

Two subsequent crystal reflections can either match (non-dispersive) or they can cross each other (dispersive set-up). Using a parallel, non-dispersive arrangement $(+n, -n)$, like the two crystal surfaces of a channel-cut crystal, the reflection domains of both crystals overlap. It was first shown by Bonse & Hart (1965) that multiple reflections in the $(+n, -n)$ non-dispersive setting from a channel-cut crystal can be used to reduce the tails of the rocking curve.

However, an effective (angle and wavelength) collimation can only be achieved in the antiparallel dispersive configuration. In order to maintain the beam position, a system of two Si-111 channel-cut crystals [C1 and C2, with each two
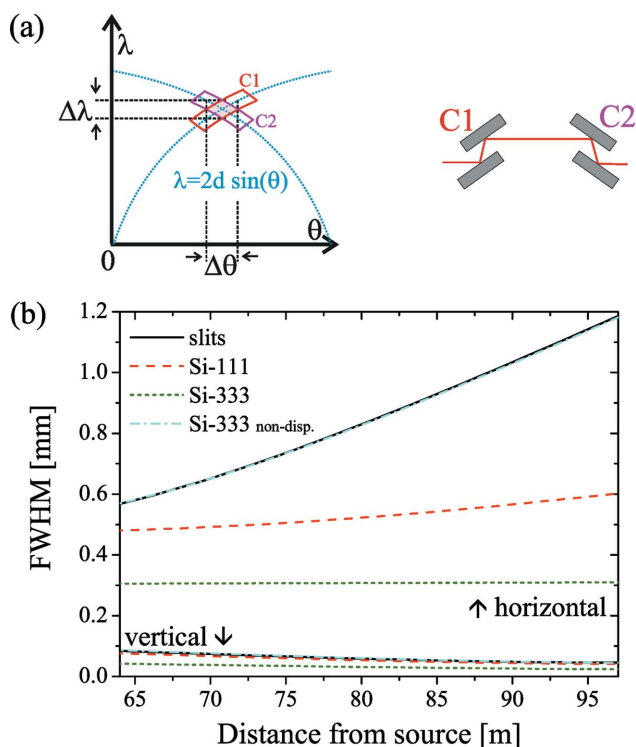
Figure 1
(*a*) The DuMond diagram of two channel-cut crystals (C1 and C2) arranged in a dispersive configuration $(+n, -n)(-n, +n)$. (*b*) Ray-tracing simulation of the reduction of angular beam divergence by using a horizontal crystal collimator at an X-ray energy of 12460 eV ($\lambda \simeq 0.0995$ nm). The beam parameters are based on beamline ID02 as indicated in Fig. 2. Calculation of the horizontal and vertical beam size (FWHM) using standard slit collimation as well as the first- and third-order reflection of a Si-111 crystal collimator are compared (dispersive set-up). Using the Si crystals in non-dispersive configuration does not change the beam profile.

symmetric reflections (Si-111 or Si-333)] arranged in a dispersive configuration (+n, −n)(−n, +n) have been chosen. This system is well known for use in high-resolution diffractometers to reduce wavelength dispersion and beam divergence (Beaumont & Hart, 1974; Bartels, 1983). In this geometry [as shown in Fig. 1(a)], the diagonal strip with negative slope represents the acceptance of the second crystal pair in anti-parallel configuration (C2). The intersection of the two diagonal strips defines the energy-angle acceptance window defined by the four-reflection system. It reduces the divergence of the exiting beam to the angular Darwin width defined by the channel-cut crystals.

2.2. Ray-tracing calculation

The influence of crystal collimation on the beam properties at the beamline ID02 has been evaluated by means of ray-tracing calculations using the *Shadow* code (Sanchez del Rio *et al.*, 2011). The main optical elements used for the calculation are visualized in Fig. 2. The X-ray source is a U21.4 undulator with small vertical size and divergence (≤20 µm and 7.6 µrad, respectively). However, the horizontal beam size is about 950 µm with a divergence of 25 µrad. A Si-111 monochromator is situated at 30 m from the source delivering a typical X-ray energy of 12460 eV ($\lambda \simeq 0.0995$ nm). A horizontally deflecting torroidal double mirror is placed at 35 m, focusing the beam onto the detector placed in the 34 m-long detector tube. The slit collimation is defined by the primary slits P1 at 27 m (aperture 0.60 mm × 0.60 mm) and secondary slits S3 at 50 m (aperture 0.15 mm × 0.20 mm). The crystal collimator is installed at 55 m from the source. After the sample position at 65 m, the beam profile was analyzed along the 34 m-long evacuated detector tube.

The ray-tracing calculations shown in Fig. 1 reveal the main improvements of the beam size and divergence in the horizontal direction. The horizontal, standard slit collimated beam (continuous line) is much larger than the vertical beam size. Introducing additionally the dispersive Si-111 crystal collimator [using the (111) reflection] considerably reduces the beam divergence (dashed line). By using the (333) reflection, the calculated beam size remains nearly constant over the observable distance range (dotted line). It can be also seen

from the graph that the use of a non-dispersive crystal collimator does not reduce the divergence of the slit-collimated beam, as discussed in the previous subsection (dash-dot line).

Regarding the vertical beam, the introduction of the crystal collimation set-up influences only slightly the vertical acceptance shortly after the collimator, but does not noticeably alter the beam profile at longer distances. However, controlling the angular acceptance of the horizontal beam by the width of the rocking curve strongly reduces the beam intensity. After four first-order reflections (Si-111), the transmission through the setup is about 26%. Using the third-order (Si-333), the transmission further drops to 0.15%.

2.3. Crystal design

For obtaining the best possible crystal surface quality, pairs of parallel crystals were fabricated instead of machining several monolithic channel-cut crystals. In this case, mechanical polishing and etching of the crystal surface is facilitated allowing a better surface finish (Sztucki *et al.*, 2008). The crystals in this so-called *pseudo channel-cut* configuration are mounted on a mechanical stage for very precise alignment. A guiding factor was the experience gained previously with a similar system to reduce the parasitic scattering in a Bonse–Hart setup (Sztucki *et al.*, 2008).

The mechanical set-up [see Fig. 3(a)] is designed in a way that it allows aligning the two crystals parallel to each other with 0.1 µrad accuracy and provides the long-term stability. For this purpose, a system with a long lever arm was designed. To reduce the space requirements, the rotation center of this tilt stage (vertical axis) is situated at the (left) border of the support. It is driven by a closed-loop picomotor actuator (Newport, Model 8310) with an encoder implemented. This guarantees the reproducibility of the rocking curve scans. An additional piezo actuator (Physik Instrumente, PI) is mounted between the tip of the picomotor and the lever arm [see inset of Fig. 3(a)]. This arrangement makes it possible to increase the resolution, at the same time keeping the lever arm short and the set-up reasonably compact. An additional tilt stage around the horizontal axis using the picomotor on top of the system (model 8302) is used for alignment of the horizontal trajectory of the beam through the channel. This tilt stage is
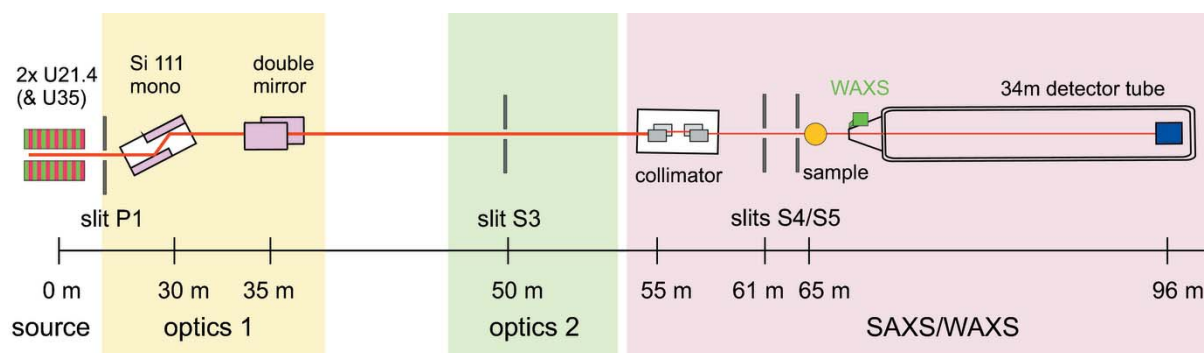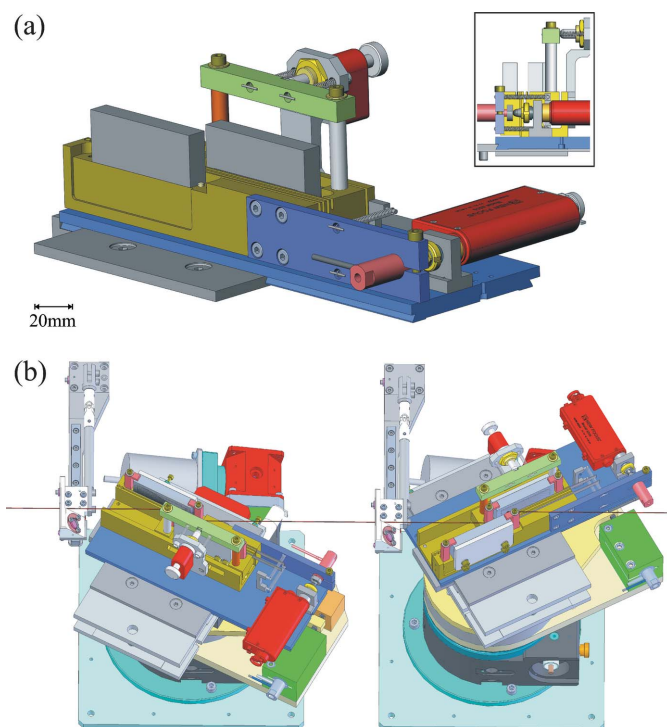

Figure 2
Sketch of the main optical elements and the 34 m-long detector tube at beamline ID02 (side view). The sample-to-detector distance can be varied between 0.8 m and 30.8 m.

(a)

20mm

(b)

Figure 3
(*a*) Design of the (pseudo channel-cut) crystal set-up. The precise and stable alignment of the Bragg condition with submicroradian accuracy of the Si-111 crystals (shown in gray) is assured by the large picomotor (Newport, red) and piezo actuator (Physik Instrumente, PI, pink) on the long lever arm (blue), which is attached to the supporting plate (yellow). Details of the arrangement are also displayed in the inset (side view): the piezo actuator (left) is directly attached to the lever arm, whereas the picomotor (right) is fixed to the supporting plate. The alignment of the horizontal trajectory of the beam through the channel is tuned by an additional small picomotor (red) pushing against a short lever arm (green) on top of the system. (*b*) Realization of the dispersive Si-111 crystal collimation set-up based on two optimized pseudo channel-cut crystals. Two beam monitors are also included. Note that the first and second sets are not identical for symmetry reasons. The beam path is indicated for the case of the Si-333 reflection.

less sensitive and mainly used for initial alignment of the set-up. The horizontal positioning of the two crystals of 65 mm length is optimized in such a way that first- and third-order reflection in an energy range between 8 keV and 20 keV are reachable. The corresponding diffraction angle spans between 5.7° and 47.9°. The standard operation is foreseen at 12460 eV, corresponding to Bragg angles of 9.1° and 28.4° for the Si-111 and Si-333 planes, respectively.

Fig. 3(*b*) shows a sketch of the realization of the dispersive crystal collimation set-up based on two well conditioned pseudo channel-cut crystals. Note that the two crystal arrangements have been designed differently for symmetry reasons: the second crystal in each pseudo channel-cut set must be mounted on the long lever arm to facilitate independent tuning of the second reflection with respect to the main rotation stage below. On the other hand, the vertical center of rotation has to be at the end of the first crystal and at the beginning of the fourth crystal to avoid a translation of the crystal when changing the reflection plane or incident energy.

This is due to the fact that the twice reflected beam is displaced by 10 mm to 15 mm depending on the Bragg angle.

The main rotation uses a Huber goniometer (model 410, coarse angular resolution of 0.001°) with piezo top section (model P401), which allows ultra-fine adjustment over a range of 0.036°. Translation stages installed between the rotation and the pseudo channel-cut crystal allow fine positioning of the center of rotation. After each pseudo channel-cut stage, a retractable arm is installed. It serves as a support for a beam monitor used during the alignment (scintillation screen with possibility of observation using a camera or a photodiode). The arm between the two crystal pairs is also equipped with a lead disk to stop the direct beam, especially the higher harmonics which have been observed to cross the corner of the first Si-111 crystal at the first Bragg reflection. The precise mechanics of the system allows reproducible alignment of the Bragg condition and requires fine tuning only once per week by scanning the piezo actuator on the long lever with the help of the retractable beam monitors.

## 3. Performance

3.1. Measured beam profile

The stability and performance of the above-described crystal collimation set-up using two Si-111 pseudo channel-cut crystals arranged in a dispersive configuration $(+n,-n)$ $(-n,+n)$ have been successfully tested at the beamline ID02 (Narayanan *et al.*, 2018). The system is installed in vacuum (10^{-5} bar) at 55 m from the source in the focused monochromatic beam (see Section 2.2 and Fig. 2). The beam profile was recorded with a 2D beam viewer (Nyquist resolution about 9.6 µm) installed in the 34 m-long detector tube between 66 m and 96 m from the source.

Fig. 4(*a*) compares the horizontal and vertical beam profiles (FWHM) with and without using the Si-333 collimation system at 96 m from the source. Parasitic slit scattering deteriorates the slit collimated beam profile especially in the horizontal direction. Using four Si-333 reflections, not only the FWHM but also the parasitic scattering in the tails around the beam in horizontal direction is considerably reduced.

Fig. 5 presents the evolution of the horizontal FWHM as a function of the distance from the source. The FWHM was determined by fitting Gaussian functions to the beam profiles. As expected, the use of the dispersive collimation system results in a considerable reduction of the horizontal divergence of the beam and its measured size remains practically constant over the accessible range of 30 m. The measured beam profiles are also in good agreement with the ray-tracing calculations presented in Fig. 1.

3.2. Comparison of resolution

The obtained resolution of the crystal collimation system for USAXS at a sample-to-detector distance of 31 m has been tested with a model system consisting of micrometre-sized spherical particles with low polydispersity. Fig. 6 presents these measurements using polystyrene latex particles
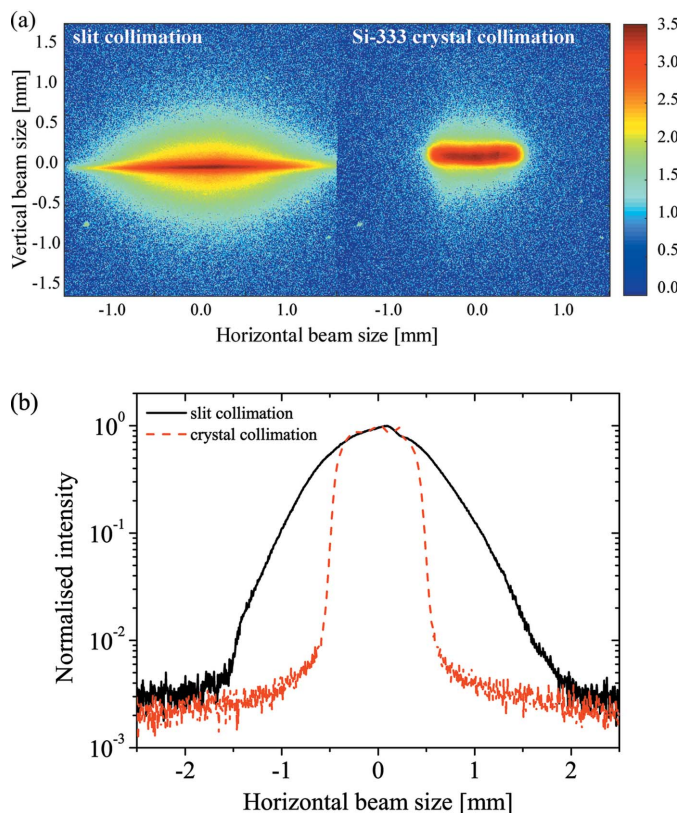
Figure 4
(*a*) Measurements of the direct X-ray beam at 96 m from the source (end of the detector tube) using a high-resolution beam viewer (Nyquist resolution about 9.6 µm). The purely slit-collimated beam on the left is noticeably larger in the horizontal direction. Additionally, the parasitic slit scattering deteriorates the beam profile more horizontally. The slit and crystal collimated beam using four Si-333 reflections is shown on the right. A clear reduction of the horizontal beam size is observed as well as the cleaning of parasitic slit scattering in that direction, resulting in an almost box-like beam profile. (*b*) A horizontal cut through the beam for the two cases displayed in (*a*).
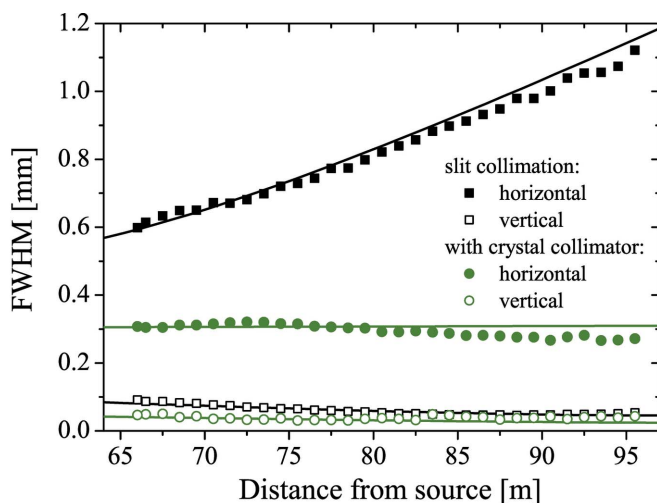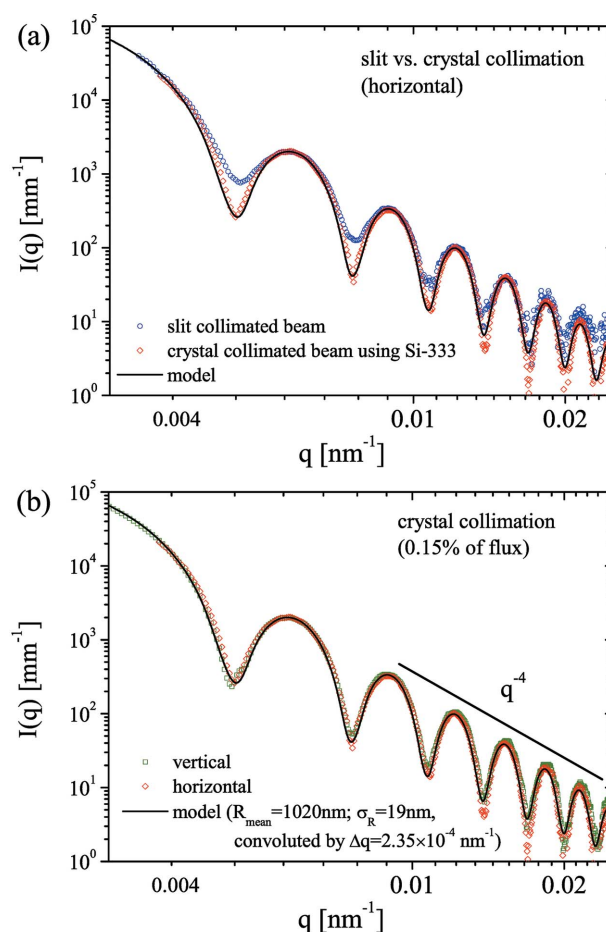

Figure 5
Measured beam profile along the 34 m detector tube using only slit collimation (rectangles) and crystal collimation with four Si-333 reflections (circles). The continuous lines correspond to the ray-tracing calculation presented in Fig. 1 for the two cases.

dispersed in a water/ethanol mixture which have been recorded in different configurations using the FReLoN detector (a fiber-optically coupled CCD detector based on the Kodak KAF-4320 image sensor) with a pixel size of about 24 µm (Narayanan *et al.*, 2018):

Configuration (A): using only slit collimation with beam-defining slits at 27 m (P1), 50 m (S3) and 61 m (S4; see Fig. 2) from the source opened by 0.2 mm × 0.2 mm, 0.1 mm × 0.1 mm and 0.12 mm × 0.2 mm, respectively. This configuration provides moderate flux ($\sim 5 \times 10^{12}$ photons s^{-1}).

Configuration (B): using additionally the Si-333 crystal collimation setup. As calculated in Section 2.2, the available flux is reduced to about 0.15% compared with configuration (A).

It has to be taken into account that the divergence of the X-ray beam at ID02 is direction dependent and that the crystal

Figure 6
Test of the collimation system by measuring USAXS profiles of micrometre-sized polystyrene latex particles (about 2 µm in diameter) with low polydispersity in a water/ethanol mixture. Panel (*a*) demonstrates the improved angular resolution in the horizontal direction (by partial integration) when comparing measurements made with a moderately slit collimated beam [configuration (A)] and using the Si-333 crystal collimator [configuration (B)]. Panel (*b*) compares the angular resolution in the vertical and horizontal direction when using Si-333 crystal collimation. Higher-order oscillations are even better resolved horizontally and the corresponding resolution is $\Delta q = 2.35 \times 10^{-4}$ nm^{-1} (continuous line).

collimator improves the performance in the horizontal direction. Therefore, data which have been normalized and averaged azimuthally $\pm 20°$ around the horizontal direction are presented in Fig. 6(a) [configurations (A) and (B)]. The increased resolution of case (B) can be easily seen as the more pronounced minima of the intensity oscillations. The best fit using the form factor of spherical particles yields a mean particle radius of 1020 nm and a standard deviation of 19 nm. The calculated polydisperse scattering curve has been convoluted with a resolution function of $\Delta q = 2.35 \times 10^{-4}\,\mathrm{nm}^{-1}$ (FWHM) in the case of the crystal collimation and $\Delta q = 6.1 \times 10^{-4}\,\mathrm{nm}^{-1}$ in the case of slit collimation (not shown). The reduced flux did not play a significant role due to sufficient scattering power of the sample except for a longer exposure time which still remained of the order of 1 s. Fig. 6(b) compares the achieved resolution in the vertical and horizontal directions for the collimation configuration (B) (Si-333 horizontal crystal collimation). The azimuthal averaging was performed in this case $\pm 20°$ around the horizontal and vertical directions. The horizontal integration which profits most from the crystal collimation shows an improved q resolution as compared with the vertical beam profile (only slit collimation). In particular, the higher-order form factor oscillations are even better resolved horizontally. Moreover, differences in the parasitic scattering of the collimated beam have to be considered. Fig. S1 of the supporting information compares the parasitic scattering with the slit- and crystal-collimated beams. The crystal-collimated beam has a much lower parasitic scattering close to the beamstop as compared with the slit-collimated beam. This is of great significance for reaching the lowest possible scattering angles in USAXS.

4. Conclusion

Highest angular resolution, not limited by scattering and diffraction-limited beam broadening, can be achieved by crystal collimation which is an interesting alternative to the commonly used pinhole collimation in SAXS for specific applications. The related loss of flux is generally not a problem due to the high brilliance of synchrotron sources and the high scattering power of typical well ordered systems, for which the high resolution is needed. A dispersive crystal collimation set-up based on two well conditioned pseudo channel-cut crystals has been developed and tested. It shows extremely good mechanical stability and reproducibility. Test measurements based on the past beam characteristics at the ESRF prove an excellent gain in resolution especially in the horizontal direction at the expense of flux, whereas slit collimation is often limited by the parasitic scattering.

Future improvements of the beam properties following the ESRF Extremely Brilliant Source upgrade will reduce the horizontal beam size and divergence by about a factor of 16 and 1.6, respectively, and make them comparable with the vertical beam parameters. With the reduction of horizontal source size, the brilliance is expected to be higher by a factor of 25 to 30. Therefore, use of the first-order Si-111 crystal collimation may not further improve the resolution, whereas the third-order reflection is still expected to reduce the horizontal beam size and divergence for applications requiring extremely high angular resolution. With the increase in brilliance, the photon flux reduction by the collimator will be significantly lower.

References

Agamalian, M., Carpenter, J. M. & Treimer, W. (2010). *J. Appl. Cryst.* **43**, 900–906.

Agamalian, M., Christen, D. K., Drews, A. R., Glinka, C. J., Matsuoka, H. & Wignall, G. D. (1998). *J. Appl. Cryst.* **31**, 235–240.

Bartels, W. J. (1983). *J. Vac. Sci. Technol. B*, **1**, 338–345.

Beaumont, J. H. & Hart, M. (1974). *J. Phys. E: Sci. Instrum.* **7**, 823–829.

Bonse, U. & Hart, M. (1965). *Appl. Phys. Lett.* **7**, 238–240.

DuMond, J. W. M. (1937). *Phys. Rev.* **52**, 872–883.

Ilavsky, J., Allen, A. J., Long, G. G. & Jemian, P. R. (2002). *Rev. Sci. Instrum.* **73**, 1660–1662.

Ilavsky, J., Jemian, P. R., Allen, A. J., Zhang, F., Levine, L. E. & Long, G. G. (2009). *J. Appl. Cryst.* **42**, 469–479.

Ilavsky, J., Shu, D., Jemian, P. R. & Long, G. G. (2007). *AIP Conf. Proc.* **879**, 1833–1836.

Kishimoto, H., Shinohara, Y., Suzuki, Y., Takeuchi, A., Yagi, N. & Amemiya, Y. (2014). *J. Synchrotron Rad.* **21**, 1–4.

Narayanan, T. (2014). *Structure from Diffraction Methods*, edited by D. W. Bruce, D. O'Hare & R. I. Walton, pp. 259–324. Chichester: Wiley.

Narayanan, T., Sztucki, M., Van Vaerenbergh, P., Léonardon, J., Gorini, J., Claustre, L., Sever, F., Morse, J. & Boesecke, P. (2018). *J. Appl. Cryst.* **51**, 1511–1524.

Petukhov, A. V., Meijer, J.-M. & Vroege, G. J. (2015). *Curr. Opin. Colloid Interface Sci.* **20**, 272–281.

Sanchez del Rio, M., Canestrari, N., Jiang, F. & Cerrina, F. (2011). *J. Synchrotron Rad.* **18**, 708–716.

Sztucki, M., Gorini, J., Vassalli, J.-P., Goirand, L., Van Vaerenbergh, P. & Narayanan, T. (2008). *J. Synchrotron Rad.* **15**, 341–349.

Sztucki, M. & Narayanan, T. (2007). *J. Appl. Cryst.* **40**, s459–s462.

Van Vaerenbergh, P., Léonardon, J., Sztucki, M., Boesecke, P., Gorini, J., Claustre, L., Sever, F., Morse, J. & Narayanan, T. (2016). *AIP Conf. Proc.* **1741**, 030034.

Zhang, F., Allen, A. J., Levine, L. E., Long, G. G., Kuzmenko, I. & Ilavsky, J. (2018). *J. Synchrotron Rad.* **25**, 1354–1361.